THE MRE INVERSE PROBLEM FOR THE ELASTIC SHEAR MODULUS*

PENNY J DAVIES†, ERIC BARNHILL‡, AND INGOLF SACK‡

Abstract. Magnetic resonance elastography (MRE) is a powerful technique for noninvasive determination of the biomechanical properties of tissue, with important applications in disease diagnosis. A typical experimental scenario is to induce waves in the tissue by time-harmonic external mechanical oscillation and then measure the tissue's displacement at fixed spatial positions 8 times during a complete time-period, extracting the dominant frequency signal from the discrete Fourier transform in time. Accurate reconstruction of the tissue's elastic moduli from MRE data is a challenging inverse problem, and we derive and analyze two new methods which address different aspects. The first of these concerns the time signal: using only the dominant frequency component loses information for noisy data and typically gives a complex value for the (real) shear modulus, which is then hard to interpret. Our new reconstruction method is based on the Fourier time-interpolant of the displacement: it uses all the measured information and automatically gives a real value of shear modulus up to rounding error. This derivation is for homogeneous materials, and our second new method (stacked frequency wave inversion, SFWI) concerns the inhomogeneous shear modulus in the time-harmonic case. The underlying problem is ill-conditioned because the coefficient of the shear modulus in the governing equations can be zero or small, and the SFWI approach overcomes this by combining approximations at different frequencies into a single overdetermined matrix–vector equation. Careful numerical tests confirm that both these new algorithms perform well.

Key words. Magnetic resonance elastography (MRE), elasticity, biomechanics, inverse problem

AMS subject classifications. 74L15, 74530, 35R30

1. Introduction.

Magnetic resonance elastography (MRE) is a powerful technique for noninvasive determination of the biomechanical properties of tissue, with important applications in disease diagnosis (as described e.g. by [17, 8, 7, 5]). Waves are induced in the tissue (typically by external mechanical excitation) and the resulting tissue displacement is measured at fixed sites *inside* it using phase-contrast MRI. This is unlike surface-based mechanical tests which can induce and measure mechanical strain only at surfaces, and thus MRE provides a far richer data source. Despite this, accurate reconstruction of the tissue's elastic moduli is still a challenging inverse problem, with many different methods proposed (see e.g. [15, 18, 17, 19, 8]).

Here we propose and analyze a new method which is based on and closely related to the recently introduced *heterogeneous multifrequency direct inversion* (HMDI) method [5]. The advantages of the new method, which we term stacked frequency wave inversion (SFWI), are that it needs only first derivatives of the wave displacement (HMDI uses second derivatives) and the shear modulus is obtained directly from a least squares solve. The "frequency domain" (time-harmonic) version of SFWI is described and analyzed in Secs. 4–5, but in practice MRE data are sampled at (typically) 8 times per time-period and the dominant frequency signal induced by the mechanical oscillations is extracted from the discrete Fourier transform (DFT) in time. The two main disadvantages of this approach are (i) that it results in a loss of information for noisy data, and (ii) using only one Fourier component typically gives a complex value for the (real) shear modulus, which is then hard to interpret. In Sec. 2 we

*Revised version: April 24, 2019.

Funding: This work was supported by the German Research Foundation (GRK2260, BIOQIC).

†Department of Mathematics and Statistics, University of Strathclyde, 26 Richmond St, Glasgow, G1 1XH, UK (penny.davies@strath.ac.uk)

‡Department of Radiology, Charité-Universitätsmedizin, Berlin, Germany (ericbarnhill@gmail.com, ingolf.sack@charite.de)

describe a new reconstruction method which is based on the Fourier time-interpolant of the displacement. It uses all the measured information and automatically gives a real value of shear modulus up to rounding error. Our derivation is for the homogeneous (constant modulus) problem and we thoroughly test it on "synthetic" and experimental data. Future work will extend the method to a SFWI algorithm for the inhomogeneous reconstruction problem, but we note that several existing methods use a "locally homogeneous" assumption (as described in e.g. [5, Sec. 1]) to which this new Fourier interpolant approach could be applied directly.

Unsurprisingly our results show that the shear modulus inverse problem is sensitive to noise in both the homogeneous and inhomogeneous case. In some sense signal denoising is the "elephant in the room" of MRE reconstruction, with published methods often being applied to highly polished data, with little information on the procedures which have been applied (note that full details of processing are given in [5]). It is clear that denoising is essential to obtain reliable results from experimental data, although it is hard to test its impact on synthetic data to which noise has been artificially added. For example, simply adding in a "random" error and then filtering it out again before running a reconstruction algorithm is unlikely to yield any insight as to the algorithm's performance on experimental data, with or without denoising. For this reason our synthetic simulations just consider the effect of added noise on the end result, rather than the effect of added noise with denoising.

It is well-known that waves are attenuated as they pass through tissue, and the absorption of energy is typically frequency-dependent (see e.g. [12]). This phenomenon can be modeled (at least for some frequency ranges) by adding in non-local terms which involve fractional derivatives in time or space. We do not consider this aspect here, focusing attention on methods to calculate parameters for the elastic wave equation. Suppose that measurements are taken in $\Omega_L \subset \mathbb{R}^d$ for $d = 2$ or 3, where L is a typical length scale – in applications Ω_L is a rectangle or box with sides of length $\mathcal{O}(L)$. The displacement $\boldsymbol{u}(\boldsymbol{x}, t)$ of an elastic material at time t of a point originally at $\boldsymbol{x} \in \Omega_L$ satisfies the momentum balance equations

$$\rho\, \ddot{\boldsymbol{u}} = \operatorname{div} T\,, \tag{1.1}$$

where ρ is the material's density, an overdot denotes the total derivative with respect to time, T is the stress tensor corresponding to the displacement $\boldsymbol{u}$, and we assume that body forces such as gravity are small enough to be ignored. The divergence of a tensor is the vector with α th component $(\operatorname{div} T)_\alpha = \partial T_{\alpha\beta}/\partial x_\beta = T_{\alpha\beta,\beta}$ (the comma denotes a space derivative), and we use the summation convention in which a repeated index (here β) means that the expression is summed from $1 : d$.

The displacement $\boldsymbol{u}$ is assumed to be small enough for a linear model to be valid, and we also assume that the material is isotropic (i.e. there is not a preferred direction, unlike muscle fibers). In this case the stress is $T_{\alpha\beta} = \lambda\, u_{\gamma,\gamma}\, \delta_{\alpha\beta} + \mu\, (u_{\alpha,\beta} + u_{\beta,\alpha})$ and (1.1) is the elastic wave equation (EWE)

$$\rho\, \ddot{u}_\alpha = \left(\mu\, (u_{\alpha,\beta} + u_{\beta,\alpha})\right)_{,\beta} + \left(\lambda\, u_{\beta,\beta}\right)_{,\alpha} \quad \text{for } \alpha = 1 : d\,, \tag{1.2}$$

where $\lambda(\boldsymbol{x})$ and $\mu(\boldsymbol{x})$ are Lamé material parameters (μ is the shear modulus).

In the homogeneous case (i.e. both λ and μ are constant) the EWE admits longitudinal and transverse plane wave solutions: a longitudinal (pressure) wave with speed $c_p = \sqrt{(\lambda + 2\mu)/\rho}$ and transverse (shear) waves with speed $c_s = \sqrt{\mu/\rho}$. Both ρ and λ are approximately constant in soft tissues – as noted in [13], traditional ultrasound imaging uses the constant value $c_p = 1540$m/s. At the typical frequencies

used in MRE (up to a few hundred Hz), this gives a wavelength of the order of several metres, which is undetectable and so longitudinal waves are removed from (1.2) in MRE applications. The Helmholtz decomposition [10] gives $\boldsymbol{u} \in \mathbb{R}^d$ for $d = 2 : 3$ as the sum of a gradient and a curl, and filtering out the gradient part of $\boldsymbol{u}$ in (1.2) gives the shear wave equation (SWE)

$$\rho\, \ddot{u}_\alpha = \left(\mu \left(u_{\alpha,\beta} + u_{\beta,\alpha}\right)\right)_{,\beta} \quad \text{for } \alpha = 1 : d\,, \tag{1.3}$$

where now $\operatorname{div} \boldsymbol{u} = 0$. We follow [15] in using this simplified version of the MRE problem, but note that it is a less accurate model than the approach of [17], where $p \equiv \lambda \operatorname{div} \boldsymbol{u}$ is taken to be an unknown pressure term and measured values of $\boldsymbol{u}$ are used to determine both μ and p from (1.2). An alternative approach using the full equation (1.2) for piecewise homogeneous materials is developed in [2].

It is known that μ varies widely in body tissues and reported values of the shear wave speed [16, Table 4] place it roughly in the range 1–20 m/s, giving a measurable wavelength at typical MRE oscillation frequencies. Our MRE reconstruction problem is then to determine the (inhomogeneous) shear modulus μ from (1.3) using space–time measurements of $\boldsymbol{u}$. As noted above, a typical experimental scenario is to vibrate the tissue at a known frequency f (for example by placing the subject on a vibrating surface), measuring $\boldsymbol{u}$ at fixed spatial positions in Ω_L at 8 time-steps per period, and the dominant frequency data is typically extracted by taking the DFT in time of the measured displacement and then fitted to the frequency domain PDE obtained by replacing $\ddot{\boldsymbol{u}}$ by $(2\pi f)^2 \boldsymbol{u}$ in (1.3). We first nondimensionalize the SWE (1.3), setting:

$$\boldsymbol{x} = L\, \tilde{\boldsymbol{x}}\,, \quad t = \tilde{t}/(2\pi\, f)\,, \quad \mu(\boldsymbol{x}) = \mu_0\, \tilde{\mu}(\tilde{\boldsymbol{x}})\,, \quad \text{and} \quad \boldsymbol{u}(\boldsymbol{x}, t) = \tilde{\boldsymbol{u}}(\tilde{\boldsymbol{x}}, \tilde{t})\,,$$

where μ_0 is a constant of the same order of magnitude as μ, so that $\tilde{\mu}(\tilde{\boldsymbol{x}})$ is an $\mathcal{O}(1)$ quantity. Dropping the tildes from all terms then gives the nondimensionalized SWE

$$\ddot{u}_\alpha = c^2\, \left(\mu \left(u_{\alpha,\beta} + u_{\beta,\alpha}\right)\right)_{,\beta} \quad \text{for } \alpha = 1 : d\,, \text{ for } (\boldsymbol{x}, t) \in \Omega_1 \times (0, 2\pi)\,, \tag{1.4}$$

where

$$c^2 = \frac{\mu_0}{\rho\, L^2 (2\pi\, f)^2}\,. \tag{1.5}$$

We derive and analyze the new SFWI method for the inhomogeneous reconstruction problem of μ from $\boldsymbol{u}$ in Secs 4–5 for the frequency domain case

$$-\, u_\alpha = c^2\, \left(\mu \left(u_{\alpha,\beta} + u_{\beta,\alpha}\right)\right)_{,\beta} \quad \text{for } \alpha = 1 : d\,, \text{ for } \boldsymbol{x} \in \Omega_1\,. \tag{1.6}$$

Before this we consider the homogeneous version of the time-dependent problem (1.4).

2. Homogeneous reconstruction problem. In the homogeneous case we set the scaling parameter μ_0 equal to the (constant) shear modulus, and the problem is then to determine the wave speed c in

$$\ddot{\boldsymbol{u}} = c^2\, \left(\nabla^2 \boldsymbol{u} + \operatorname{grad}\left(\operatorname{div} \boldsymbol{u}\right)\right) \tag{2.1}$$

from data measurements, and then μ_0 follows from (1.5). Note that we have assumed that $\operatorname{div} \boldsymbol{u} = 0$ in the derivation of (1.3) from (1.2), but we explicitly include the final term in (2.1) because the corresponding term in the inhomogeneous equation (1.4) is nonzero. Keeping the equation in this form also makes it easier to see how the pressure term in the more accurate model of [17] could be incorporated.

The displacement $\boldsymbol{u}$ in MRE reconstructions is typically sampled at 8 times per time-period (which is far too coarse a timestep to use in a central difference approximation of $\ddot{\boldsymbol{u}}$ in (2.1)) and it is standard practice to take its DFT and use the Fourier component which corresponds to the underlying oscillation frequency. This throws away potentially useful information and typically gives a complex value of the real quantity μ_0, and instead we derive a new MRE inversion procedure which uses Fourier interpolation in time. The new method is extensively tested on "synthetic" problems in 1D and 2D space and also used for 3D MRE data in Sec 3.

2.1. Homogeneous problem in 1D. The 1D model problem is to find $c_{\rm sq} \approx c^2$ to best fit measured values of the 2π-periodic in time function $u(x,t)$ which satisfies the underlying equation

$$u_{tt} = c^2\, u_{xx}\,, \quad x \in (0,1)\,. \tag{2.2}$$

Our strategy is to replace u in (2.2) by its (time) Fourier interpolant, and we first describe this construction, which follows the approach of Trefethen [20], before detailing the full approximation method for $c_{\rm sq}$.

Fourier interpolant in time. Suppose that $v \in C[0,2\pi]$ is a 2π-periodic function measured at $t_m = mh$ for $m = 0:M-1$ where $h = 2\pi/M$, and set $v^m = v(t_m)$. The discrete Fourier transform (DFT) of v is $\left\{\widehat{v}^\ell \;:\; \ell = -M/2+1 : M/2\right\}$, where

$$\widehat{v}^\ell = \sum_{m=0}^{M-1} e^{-i\ell t_m}\, v^m\,, \quad \ell = -M/2+1 : M/2$$

and the inverse DFT is

$$v^m = \frac{1}{M} \sum_{\ell=-M/2}^{M/2\,\prime} e^{i\ell t_m}\, \widehat{v}^\ell\,, \quad m = 0 : M-1\,,$$

where $\widehat{v}^{-M/2} = \widehat{v}^{M/2}$ and the prime on the sum indicates that terms with $\ell = \pm M/2$ are multiplied by $\frac{1}{2}$. The Fourier interpolant of v is $V(t)$ defined by

$$V(t) = \frac{1}{M} \sum_{\ell=-M/2}^{M/2\,\prime} e^{i\ell t}\, \widehat{v}^\ell\,.$$

It is an analytic function of t and $V(t_m) = v(t_m)$ for each m by construction. Differentiating twice in time at $t = t_m$ gives

$$\ddot{V}(t_m) = \frac{1}{M} \sum_{\ell=-M/2+1}^{M/2} \left(-\ell^2\right)\, e^{i\ell t_m}\, \widehat{v}^\ell\,, \quad m = 0 : M-1\,. \tag{2.3}$$

As noted in [20, Ch. 3], if the way the DFT is implemented assumes a different ordering of the wavenumbers then the vector of multipliers of the components $-\ell^2$ will also need to be reordered. For example, if using MATLAB's `fft` function to overwrite the M-component data vector v, then the vector of multipliers of the components $e^{i\ell t_m}$ in (2.3) is given by the command `-lsq.*v` where `lsq = [0:M/2,-M/2+1:1].^2`. Other implementations may require a different ordering.

Least squares approximation of c^2. The measured displacement is the average value over a voxel, and so in 1D space it corresponds to the average over an interval of length $\Delta x = 1/J$, i.e. the measurement $u_j^m \approx u(x_{j-1/2}, t_m)$, where $x_r = r\Delta x$. Approximating u in (2.2) by its Fourier interpolant U at each space–time measurement point $(x_{j-1/2}, t_m)$ and U_{xx} by a second central difference gives

$$\frac{1}{M} \sum_{\ell=-M/2+1}^{M/2} \left(\ell^2 \, \widehat{u}_j^\ell + c^2 \, \frac{\delta_{11}}{\Delta x^2} \, \widehat{u}_j^\ell \right) e^{i\ell t_m} \approx 0 \quad \text{for each } m \text{ and } j \,,$$

where $\delta_{11}\, g_j = g_{j+1} - 2\, g_j + g_{j-1}$. Hence $c_{\rm sq} \approx c^2$ is the best least squares solution of

$$\ell^2 \, \widehat{u}_j^\ell + c_{\rm sq} \, \frac{\delta_{11}}{\Delta x^2} \, \widehat{u}_j^\ell = 0 \quad \text{over } \ell \text{ and } j \,.$$

To calculate $c_{\rm sq}$ we multiply this expression by the complex conjugate $\overline{\widehat{u}}_j^\ell$ and sum over all indices j for which the term $\delta_{11}\, \widehat{u}_j^\ell$ makes sense ($j = 2 : J-1$) to give the least squares problem:

$$\text{find } c_{\rm sq} \approx c^2 \text{ to minimize } \|\boldsymbol{a}\, c_{\rm sq} - \boldsymbol{b}\| \,, \tag{2.4}$$

where $\boldsymbol{a}$, $\boldsymbol{b} \in \mathbb{R}^M$ have components

$$a_\ell = -\sum_{j=2}^{J-1} \left(\frac{\delta_{11}}{\Delta x^2} \, \widehat{u}_j^\ell \right) \overline{\widehat{u}}_j^\ell \,, \quad b_\ell = \ell^2 \sum_{j=2}^{J-1} \left| \widehat{u}_j^\ell \right|^2 \quad \text{for } \ell = -M/2+1 : M/2 \,. \tag{2.5}$$

In practice (using floating point arithmetic) it can be more accurate to use "summation by parts" to replace the first sum by the product of first differences:

$$-\sum_{j=2}^{J-1} \left(\frac{\delta_{11}}{\Delta x^2} \, \widehat{u}_j^\ell \right) \overline{\widehat{u}}_j^\ell = \sum_{j=2}^{J-2} \left| D\widehat{u}_j^\ell \right|^2 + D\widehat{u}_1^\ell \, \frac{\overline{\widehat{u}}_2^\ell}{\Delta x} - D\widehat{u}_{J-1}^\ell \, \frac{\overline{\widehat{u}}_{J-1}^\ell}{\Delta x} \,, \tag{2.6}$$

where $D\,\widehat{u}_j^\ell = \left(\widehat{u}_{j+1}^\ell - \widehat{u}_j^\ell \right) / \Delta x$. We always do this, but because the formula for a term like a_ℓ is far simpler written as a second difference (especially in higher space dimensions), we will not in general give the equivalent first difference form explicitly.

Note that the approximation $c_{\rm sq}^*$ of c^2 given by the Helmholtz approach (1.6) is obtained from a single Fourier component of (2.4) rather than the least squares solution over all M Fourier components, i.e. it is

$$c_{\rm sq}^* = b_{\ell^*} / a_{\ell^*} \tag{2.7}$$

for the dominant frequency ℓ^*.

2.2. Homogeneous problem in 2D. The 2D homogeneous model problem uses measured values of $\boldsymbol{u} \in \mathbb{R}^2$ in (2.1) to determine $c_{\rm sq} \approx c^2$. We use a similar approach as for 1D: find an exact 2π-periodic in time solution of (2.1); add synthetic noise; approximate the (noisy) $\boldsymbol{u}$ in time by its Fourier interpolant and approximate the space derivatives in (2.1) by finite differences; and construct a least squares approximation $c_{\rm sq}$ of c^2. We use square pixels of side $\Delta x = 1/J_1$ on a $J_1 \times J_2$ spatial grid and as in 1D we approximate the two spatial components of $\boldsymbol{u}$ in time by their Fourier interpolants and use second central difference operators to approximate $\partial_{\alpha\alpha}$

terms. The approximation used for mixed partial derivatives is $\partial_{12}\, g \approx \delta_{12}\, g/\Delta x^2$, where

$$\delta_{12}\, g_{p,q} = \left[g_{p+1,q+1} - g_{p-1,q+1} - (g_{p+1,q-1} - g_{p-1,q-1})\right]/4\,.$$

Using these approximations in (2.1) leads to an expression like (2.6) for each spatial component of $\boldsymbol{u}$ and taking the scalar product with the complex conjugate of $\left(\widehat{u}^{\ell}_{1[j,k]},\, \widehat{u}^{\ell}_{2[j,k]}\right)$ and summing over $j = 2 : J_1 - 1$ and $k = 2 : J_2 - 1$ again gives the least squares problem (2.4) for $c_{\rm sq} \approx c^2$, where now for each ℓ we have $a_\ell = a^{[1]}_\ell + a^{[2]}_\ell$ for

$$a^{[1]}_\ell = \frac{-1}{\Delta x^2} \sum_{j=2}^{J_1-1} \sum_{k=2}^{J_2-1} \left(2\,\delta_{11}\, \widehat{u}^{\ell}_{1[j,k]} + \delta_{22}\, \widehat{u}^{\ell}_{1[j,k]} + \delta_{12}\, \widehat{u}^{\ell}_{2[j,k]}\right)\, \overline{\widehat{u}}^{\ell}_{1[j,k]}\,,$$

$$a^{[2]}_\ell = \frac{-1}{\Delta x^2} \sum_{j=2}^{J_1-1} \sum_{k=2}^{J_2-1} \left(\delta_{11}\, \widehat{u}^{\ell}_{2[j,k]} + 2\,\delta_{22}\, \widehat{u}^{\ell}_{2[j,k]} + \delta_{12}\, \widehat{u}^{\ell}_{1[j,k]}\right)\, \overline{\widehat{u}}^{\ell}_{2[j,k]}\,,$$

$$\text{and} \quad b_\ell = \sum_{j=2}^{J_1-1} \sum_{k=2}^{J_2-1} \left(\left|\widehat{u}^{\ell}_{1[j,k]}\right|^2 + \left|\widehat{u}^{\ell}_{2[j,k]}\right|^2\right)\,.$$

3. Numerical results for the homogeneous problem. We now present numerical test results for the time-dependent homogeneous problem. We use 'synthetic' data (with and without added noise) in one and two space dimensions and unsmoothed MRE measurements in 3D. The simplicity of the 1D case allows the algorithm to be extensively tested, with and without added noise, revealing insights that are useful for higher space dimensions. It is well-known that noisy MRE data can cause the computed solution to be severely underestimated (see e.g. [4]), and we investigate how this depends on the underlying wave speed.

3.1. Results for synthetic 1D data. The function $u(x,t) = \cos(t + x/c)$ is an exact 2π-periodic solution of (2.2), and we consider a noisy version of it setting

$$u^m_j = \cos(t_m + x_{j-1/2}/c) + \varepsilon^m_j\,, \quad j = 1 : J,\ m = 0 : M-1\,, \tag{3.1}$$

where each $\varepsilon^m_j \in [-\varepsilon, \varepsilon]$ for $0 \le \varepsilon \le 0.1$ is a pseudo-random error term to simulate experimental error. We use these values of u^m_j to calculate the vectors $\boldsymbol{a}$ and $\boldsymbol{b}$ in (2.5) and then find $c_{\rm sq} \approx c^2$ which satisfies (2.4). The absolute error in c^2 is $\mathcal{E}_A = c_{\rm sq} - c^2$, and the relative error is $\mathcal{E}_R = \mathcal{E}_A/c^2$.

We first examine the behavior of the calculated value $c_{\rm sq}$ with no added noise (i.e. (3.1) with $\varepsilon = 0$). In this case u is analytic and $M = 8$ is enough to capture its complete time behavior, and the calculated value $c_{\rm sq}$ does not change as M is increased. Figure 3.1 illustrates the behavior of $c_{\rm sq}$ with $J = 1/\Delta x$ – the leading term of the absolute error is $\Delta x^2/12$ and further investigation indicates $\mathcal{E}_A \approx \Delta x^2/12 + \alpha\, \Delta x^4/c^2$ for a (real) constant α independent of both c and J.

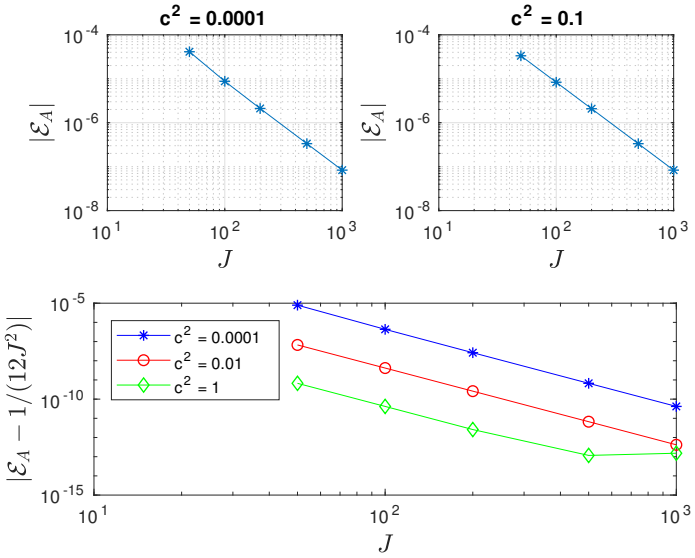

FIG. 3.1. *Error plots for c_{sq} reconstructed from the data (3.1) with $\varepsilon = 0$ and $M = 8$.*

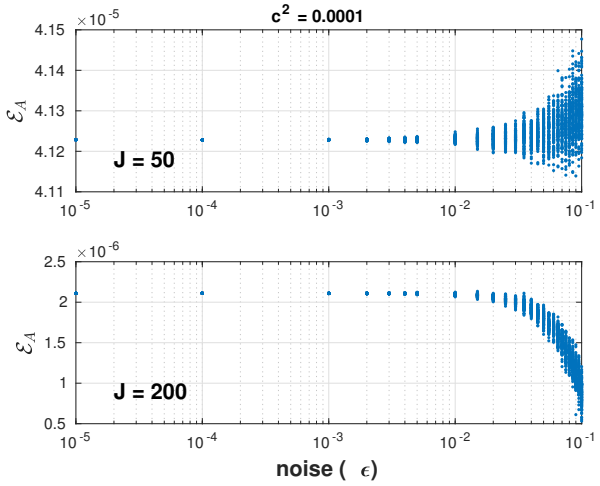

FIG. 3.2. *Absolute error $\mathcal{E}_A$ with $c^2 = 10^{-4}$ and $M = 8$ for 100 simulations at each synthetic noise level ε.*

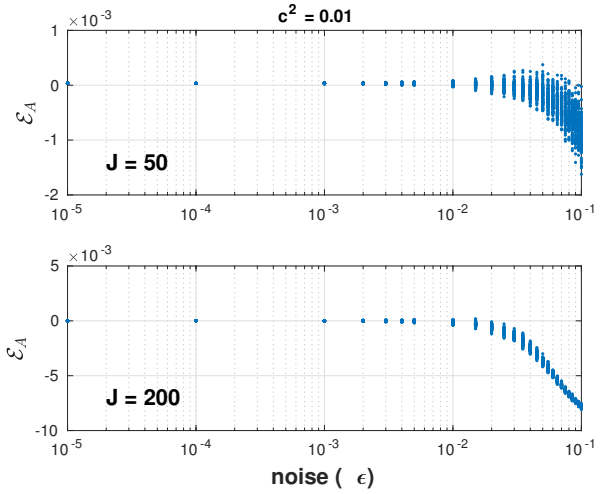

FIG. 3.3. *Absolute error $\mathcal{E}_A$ with $c^2 = 10^{-2}$ and $M = 8$ for 100 simulations at each synthetic noise level ε.*

When $\varepsilon > 0$ the underlying function u is no longer analytic, but increasing M still makes very little difference to the reconstruction accuracy and we fix $M = 8$. The dependence of the absolute error $\mathcal{E}_A$ on J and ε is illustrated in Figs 3.2–3.3, and each plot shows $\mathcal{E}_A$ at 100 simulations for a given noise level ε, calculated directly from the data (3.1) with no filtering or smoothing. When ε is small compared with Δx, then the results are similar to the $\varepsilon = 0$ case above with $\mathcal{E}_A = \mathcal{O}(\Delta x^2)$, but $|\mathcal{E}_A|$ increases rapidly with increasing noise level ε, and typically then behaves worse as the mesh is refined (because the approximation error in the first derivative terms $D\,\widehat{u}_j^{\ell}$ in (2.5) is proportional to $\varepsilon/\Delta x$). The onset of this rapid growth of $|\mathcal{E}_A|$ with ε depends on c^2, with small values of c^2 (corresponding to a high spatial wavelength) giving better results. For example, the error when $c^2 = 10^{-4}$ reduces as J is increased (the bottom plot of Fig. 3.2 shows a 1% relative error at 10% noise), whereas when $c^2 = 10^{-2}$ the error is about ten times larger when $J = 200$ than it is at $J = 50$. In all cases the rapidly growing error corresponds to an **underestimate** of the true solution. It is well-known in the MRE community that noisy data causes the shear modulus to be underestimated (see e.g. [4]), and our simulations allow this to be quantified. Fixing $J = 100$ and $M = 8$, we calculate the average value of $c_{\rm sq}$ over 100 runs at each of a set of noise levels $\varepsilon \le 1$ and wave speeds $c^2 = 10^{-k}$ for $k = 0 : 4$. The 'critical' noise level $\varepsilon_{\rm cr}$ at each wave speed is defined to be that at which the relative error in $c_{\rm sq}$ first reaches 0.1 (i.e. 10%), and a log–log plot of $\varepsilon_{\rm cr}$ against c^2 (see Fig. 3.7) shows that $\varepsilon_{\rm cr} \approx A_1\, c^{-1}$ for A_1 independent of c.

Note that the formulation (2.4) automatically gives a real value of $c_{\rm sq}$ (up to rounding error), but this is **not** true for $c_{\rm sq}^*$ given by (2.7). Although the scatter plots for the error in the real part of $c_{\rm sq}^*$ look qualitatively similar to Figs 3.2–3.3, the ratio of the imaginary and real parts of $c_{\rm sq}^*$ in these simulations can vary significantly. For example, Fig. 3.4 shows this ratio plotted against ε when $c^2 = 0.01$ – it ranges from 10^{-5} to 10^3. A high ratio makes the calculated value of $c_{\rm sq}$ (and hence μ_0) very hard to interpret.

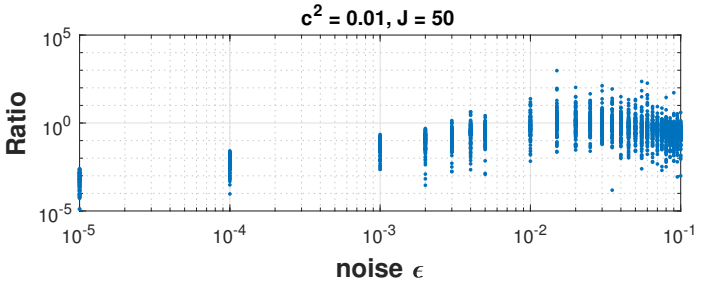

FIG. 3.4. *Ratio of the imaginary and real parts of the absolute error in c_{sq}^* when $c^2 = 10^{-2}$, $J = 50$ and $M = 8$ for 100 simulations at each synthetic noise level ε.*

3.2. Results for synthetic 2D data. The 1D solution $\boldsymbol{u}(\boldsymbol{x}, t) = (\cos(t + x_1/(c\sqrt{2})), 0)^T$ also satisfies the 2D version of (2.1), but we now investigate fully 2D solutions with and without added noise. The function $\boldsymbol{u}(\boldsymbol{x}, t) = \boldsymbol{r}\,\cos(t + \boldsymbol{\nu}\cdot\boldsymbol{x}/c)$ satisfies (2.1) when $\boldsymbol{\nu} = (\cos\theta, \sin\theta)$ and $\boldsymbol{r} = (\sin\theta, -\cos\theta)$ for any incidence angle θ. The rectangular space domain is $\boldsymbol{x} \in [0, R_1] \times [0, R_2]$, where we set $R_1 = 1$ (so L in (1.5) is the x_1-length of Ω_L). It is typical for MRE measurements to use square rather than rectangular pixels in the xy-plane. Numerical tests indicate that the method's behavior on rectangular pixels is as would be expected from the 1D and square 2D

results, and for simplicity we only present results for square pixels. The measured displacement is then the average value over a square of side Δx where $\Delta x = 1/J_1$ and we record it at the midpoint, setting

$$u_{\alpha[j,k]}(t_m) = r_\alpha \cos\left(t_m + \frac{\boldsymbol{\nu}\cdot\boldsymbol{x}_{j-1/2,k-1/2}}{c}\right) + \varepsilon^m_{j,k}\,,$$

where $\boldsymbol{x}_{r,s} = (r\,\Delta x, s\,\Delta x)$, $R_2 = J_2\,\Delta x$ and each $\varepsilon^m_{j,k} \in [-\varepsilon, \varepsilon]$ is an added noise term to simulate experimental error.

We first examine the dependence of the absolute error $\mathcal{E}_A$ on the space mesh size Δx and incidence angle θ with no added noise ($\varepsilon = 0$). The results do not appear to depend on c^2 or the domain's aspect ratio R_2/R_1, and a sample plot is shown in Fig. 3.5. The leading term of the error is again proportional to Δx^2, with a constant of proportionality which is independent of c^2 but it does depend on θ. This is because the effective mesh spacing "seen" by the wave depends on its incidence angle – if it is aligned with the mesh ($\theta = 0$ or $\pi/2$) then the perpendicular distance between consecutive mesh points is Δx, but if $\theta = \pi/4$ then the mesh points are aligned diagonally and their perpendicular distance appears to be $\Delta x/\sqrt{2}$ apart. See e.g. [9] for more information on wave propagation through anisotropic meshes.

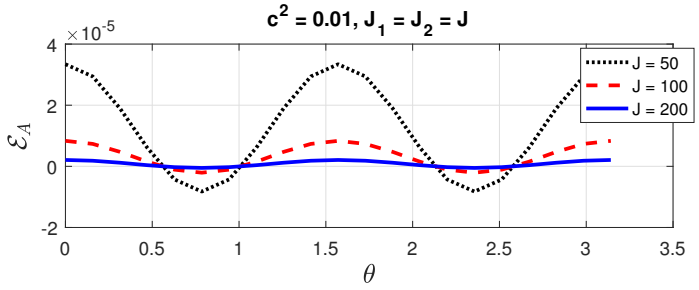

FIG. 3.5. *Absolute error $\mathcal{E}_A$ against incidence angle θ for a unit square of mesh size $\Delta x = 1/J$ when $c^2 = 10^{-2}$ and $M = 8$.*

Fig. 3.6 shows $\mathcal{E}_A$ at 100 simulations for a given noise level ε, calculated from unsmoothed data at incidence angle $\theta = 1.3$, and using $M = 8$ and $J_1 = J_2 = 100$ at two values of c^2. These 2D errors are more tightly clustered at each noise level than the similar 1D plots in Figs. 3.2–3.3 and for small values of ε there is a small positive error $\mathcal{E}_A$. As in 1D the error drops through zero as ε increases, rapidly becoming large and negative – the bottom plot shows a relative error of $\mathcal{E}_R \approx 0.8$ (i.e. 80%) when $\varepsilon = 0.1$ (10% noise). The size of the relative error depends on c^2, with lower speeds (higher spatial frequencies) giving better results, again as in 1D. E.g. a 10% noise level corresponds to about a 20% relative error when $c^2 = 10^{-3}$, and noise levels of more than 10% are needed to show this behavior when $c^2 = 10^{-4}$. The relationship between the error and noise is illustrated in Fig. 3.7; as for the 1D simulations we set $J_1 = J_2 = 100$, $M = 8$ and calculate the average value of $c_{\rm sq}$ over 100 runs at each of a set of noise levels $\varepsilon \le 1$ and wave speeds $c^2 = 10^{-k}$ for $k = 0:4$. The 'critical' noise level $\varepsilon_{\rm cr}$ at each wave speed shown in the Figure is again that at which the relative error in $c_{\rm sq}$ first reaches 0.1, and the 2D results are $\varepsilon_{\rm cr} \approx A_2\,c^{-1}$ where the constant A_2 is almost exactly half the 1D constant A_1. In both 1D and 2D the relative error is very sensitive to increasing noise, with the calculated value $c_{\rm sq}$ rapidly decreasing for $\varepsilon > \varepsilon_{\rm cr}$.

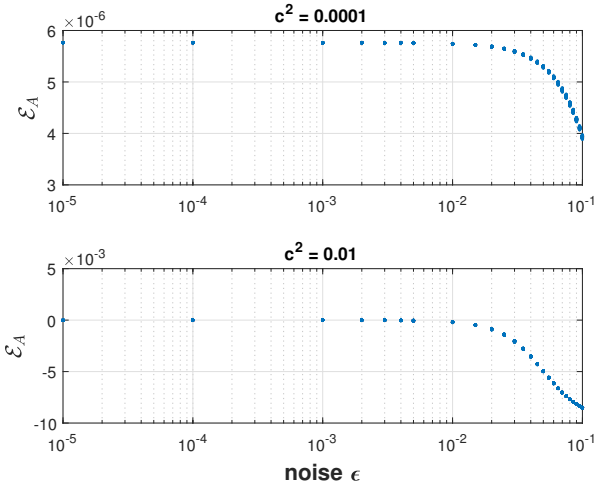

FIG. 3.6. *Absolute error $\mathcal{E}_A$ for a unit square of mesh size $\Delta x = 0.01$ when $\theta = 1.3$ and $M = 8$ for 100 simulations at each synthetic noise level ε with $c^2 = 10^{-4}$ (top) and $c^2 = 10^{-2}$ (bottom).*

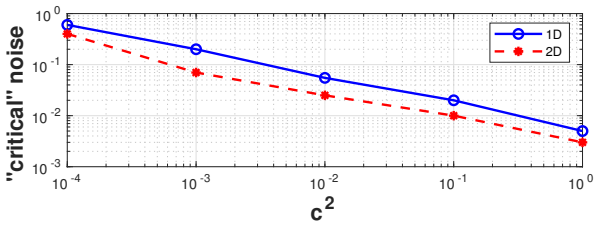

FIG. 3.7. *Critical noise level ε_{cr} at which $\mathcal{E}_R$, the relative error in c_{sq}, first becomes 10% plotted against c^2 for the 1D and 2D simulations. See text for details of the parameters used.*

3.3. Homogeneous problem in 3D. The physical problem for which we have experimental displacement values is that of a cube of size $95 \times 95 \times 95$ mm^3 of homogeneous ultrasound gel whose density is close to that for water, which is vibrated at a constant frequency f. Full details of the experimental procedure are given in [7]. Eight ($M = 8$) measurements are taken per time period at frequencies $f = 30 : 5 : 60$ Hz, giving seven experimental runs in total. The voxel dimensions are $1 \times 1 \times 2$ mm, and the full data set covers $128 \times 96 \times 21$ voxels (and hence includes "noise" measurements in the air as well as measurements from within the cube). Our calculations are based on a data subset of $N_v = 75 \times 68 \times 21$ voxels giving the x_1 physical length $L = 75$ mm. The measured displacements are nondimensionalized as described in Sec. 1, with the three components of $\boldsymbol{u}(\cdot, t_m)$ assumed to be at the center of each voxel for $m = 0 : M - 1$. These samples are all raw data which has not been smoothed, but have been "unwrapped" (from an acquisition in an interval of length 2π) by the Laplacian unwrapper – this suppresses constant offsets or first order gradients (details are given in [7]).

The algorithm for calculating $c_{\text{sq}} \approx c^2$ from 3D data values is an obvious extension of that in 2D, but now the terms a_ℓ and b_ℓ are summed over three spatial indices. Before presenting results on c_{sq} we first briefly discuss how to evaluate the quality of the data.

Analysis of data quality. The time behavior of perfect (nondimensionalized) data at a fixed point in space takes the form $v(t) = A + \cos(t + B)$ for constants A and B. Measuring it at t_m, $m = 0 : M-1$ and taking its DFT as described in Sec. 2.1 gives the M-component complex vector $\widehat{\boldsymbol{v}}$ where $\widehat{v}^{\pm 1}$ are complex conjugates which contain the signal information, $\widehat{v}^0$ depends on the translation A and the remaining $M-3$ components $\widehat{v}^\ell$ for $|\ell| > 1$ are all zero. Thus the quantity

$$\frac{1}{(M-3)|\widehat{v}^1|} \sum_{|\ell|>1} |\widehat{v}^\ell|$$

gives an indication of how "good" (i.e. how close to exact periodic) the data values are. This is important because equations (2.4) and (1.6) are both derived under the assumption that the measurements are time-periodic. If this is far from being the case, then it is unclear what the calculated values c_{sq} or c^*_{sq} actually mean. For each data run we sum up this quality indicator for the three spatial components of $\boldsymbol{u}$ at all voxels and divide by the total number of terms $(3 \times N_v)$ to obtain the "quality index", which is a measure of the signal-to-noise ratio (SNR). It is plotted in Fig. 3.8 (top) against (physical) oscillation frequency f: the measurements at 50 Hz appear to be closest to being periodic. Note that there are other ways to evaluate the SNR, for more information see e.g. [4].

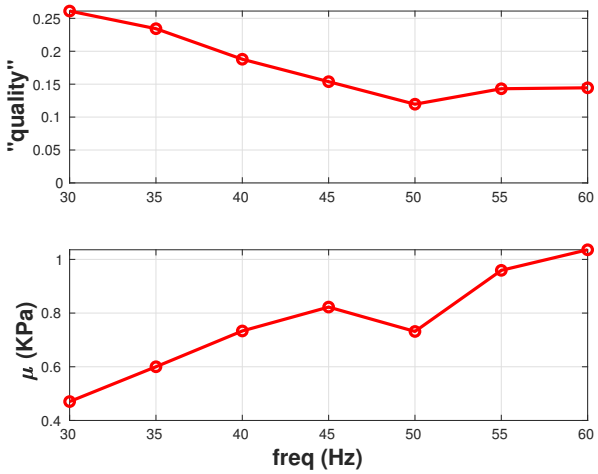

FIG. 3.8. TOP: *Quality index against (physical) frequency f.* BOTTOM: *Calculated value of (physical) μ_0 against f. Our results are consistent with those (calculated from rheometric data) given in [7, Fig. 4].*

Results. We exclude the component with $\ell = 0$ in the 3D analogue of (2.5)) in the least squares calculation for experimental data. It is a zero-frequency (constant) mode for which $b_0 = 0$ by definition and a_0 should also be zero because all its terms involve second differences applied to a constant. Fig. 3.8 (lower) shows the calculated value of the physical shear modulus μ_0 at each experimental run. This is consistent with the values of μ_0 (called $|G^*|$) calculated for this type of gel from rheometric data given in [7, Fig. 4]. For example, the "most periodic" sample at 50 Hz gives $\mu_0 = 0.73$ KPa, which is within the error bars given in [7] for the rheometric measurements.

4. Inhomogeneous problem: stacked frequency wave inversion. We now describe and analyze our new SFWI method for the *inhomogeneous* MRE reconstruc-

tion problem. For simplicity we restrict attention to the frequency domain version (1.6), rather than (1.4). The nondimensionalized function $\mu(\boldsymbol{x})$ in (1.6) is an $\mathcal{O}(1)$ quantity, and we look at examples in which it is piecewise constant, with inclusions of $\mu > 1$ embedded in a background material for which $\mu = 1$. We rewrite (1.6) as

$$-\omega^2 u_\alpha = (\mu\,(u_{\alpha,\beta} + u_{\beta,\alpha}))_{,\beta} \quad \text{for } \alpha = 1:d\,, \text{ for } \boldsymbol{x} \in \Omega_1\,, \tag{4.1}$$

where the nondimensionalized frequency is $\omega = 2\pi f L\sqrt{\rho/\mu_0}$. As in Sec. 2 we analyze the problem in 1D and 2D space, with numerical test results given in Sec. 5; 3D results for the related HMDI method are presented in [5].

4.1. SFWI in 1D space. The 1D model problem is to find $\mu(x)$ given the nondimensionalized frequency ω and measured values of $u(x)$ such that

$$-\omega^2 u = (\mu\, u')'\,, \quad x \in (0,1)\,, \tag{4.2}$$

where $'$ denotes d/dx. This is a first order ODE in μ, which needs one other piece of information, such as a boundary condition, in order to give a unique solution. For example, if $u_k(x)$ are measurements at ω_k for $k = 1:2$ with both $u_k'(0) \neq 0$, then the general solution of (4.2) can be written as

$$\mu(x)\, u_k'(x) = \mu(0)\, u_k'(0) - \omega_k^2 \int_0^x u_k(s)\, ds$$

and $\mu(0)$ can be eliminated to obtain $\mu(x)$ in terms of the u_k. However this is not a practical solution method for noisy data (it gives an ill-conditioned set of equations and poor results). The SFWI approach overcomes this by combining approximations of (4.2) at different frequencies into a single overdetermined matrix–vector equation (see also [3]). Our underlying approximation of (4.2) uses finite volumes based on a staggered grid (u and μ are recorded at different grid points), as illustrated in Fig. 4.1. The measured displacement is the average over an interval of length $\Delta x = 1/J$, and u is regarded as being measured at interval midpoints (blue stars). The μ grid points are interior interval endpoints, i.e. $\mu_j \approx \mu(x_j)$ for $j = 1:J-1$ (red circles).

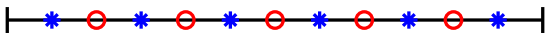

FIG. 4.1. *Staggered grid for 1D approximation of (4.2) on* $[0,1]$*: the grid points for* u *are denoted by blue stars, and those for* μ *by red circles*

Equation (4.2) is integrated between each pair of red circles to give

$$[\mu(x)\, u'(x)]_{x_j}^{x_{j+1}} = -\omega^2 \int_{x_j}^{x_{j+1}} u(x)\, dx\,, \quad j = 1:J-2\,. \tag{4.3}$$

Then using a central difference approximation for the derivative u' and the midpoint rule to approximate the integral term gives the underdetermined linear system

$$A\,\boldsymbol{\mu} = \boldsymbol{b} \tag{4.4}$$

for $\boldsymbol{\mu} = (\mu_1, \ldots, \mu_{J-1})^T$, where $b_j = \omega^2\, \Delta x\, u(x_{j+1/2})$ for $j = 1:J-2$ and $A \in \mathbb{R}^{(J-2)\times(J-1)}$ is the bidiagonal matrix with entries

$$A = \begin{pmatrix} a_1 & -a_2 & 0 & 0 & \ldots & 0 & 0 \\ 0 & a_2 & -a_3 & 0 & \ldots & 0 & 0 \\ \vdots & \vdots & \ddots & \ddots & \ddots & \ddots & \vdots \\ 0 & 0 & 0 & 0 & \ldots & a_{J-2} & -a_{J-1} \end{pmatrix}$$

with $a_j = \big(u(x_{j+1/2}) - u(x_{j-1/2})\big)/\Delta x \approx u'(x_j)$.

We first investigate the structure of the linear system (4.4), summarizing the key results below.

LEMMA 4.1. *The matrix A in (4.4) has the following properties.*

1. *AA^T is invertible on its range, $\mathcal{R}(AA^T)$.*
2. *Equation (4.4) has a solution if and only if $\boldsymbol{b} \in \mathcal{R}(AA^T)$, and if $\boldsymbol{b} \in \mathcal{R}(AA^T)$ then the general solution of (4.4) is*

$$\boldsymbol{\mu} = A^T \boldsymbol{z} + \boldsymbol{\nu}\,, \tag{4.5}$$

where $\boldsymbol{z} \in \mathbb{R}^{J-2}$ is the unique solution of $AA^T\boldsymbol{z} = \boldsymbol{b}$ and $A\boldsymbol{\nu} = \boldsymbol{0}$.

The proof is straightforward using the following standard result:

THEOREM 4.2 (Decomposition; see e.g. [14]). *Suppose that $B \in \mathbb{R}^{m\times n}$ with $m \le n$. Then $\mathbb{R}^n$ is the direct sum of the range of B^T and the null space of B, i.e.*

$$\mathbb{R}^n = \mathcal{R}(B^T) \oplus \mathcal{N}(B)\,. \tag{4.6}$$

Proof of Lemma 4.1.

1. Suppose that $AA^T\boldsymbol{z} = \boldsymbol{0}$ for some $\boldsymbol{z} \in \mathcal{R}(AA^T)$. Then $\boldsymbol{z} \in \mathcal{R}(AA^T) \cap \mathcal{N}(AA^T) = \{\boldsymbol{0}\}$ by applying Theorem 4.2 to $B = AA^T$. Thus AA^T is invertible on $\mathcal{R}(AA^T)$.
2. It follows from Theorem 4.2 that $\mathbb{R}^{J-1} = \mathcal{R}(A^T) \oplus \mathcal{N}(A)$, and so if $\boldsymbol{\mu} \in \mathbb{R}^{J-1}$ then $\boldsymbol{\mu} = A^T\boldsymbol{z} + \boldsymbol{\nu}$ for some $\boldsymbol{z} \in \mathbb{R}^{J-2}$ and $\boldsymbol{\nu} \in \mathcal{N}(A)$. Hence $A\boldsymbol{\mu} = AA^T\boldsymbol{z}$, and if $\boldsymbol{b} \notin \mathcal{R}(AA^T)$ then (4.4) cannot have a solution. If $\boldsymbol{b} \in \mathcal{R}(AA^T)$ then invertibility of AA^T guarantees a unique solution $\boldsymbol{z}$ of $AA^T\boldsymbol{z} = \boldsymbol{b}$. ∎

Characterizing $\mathcal{N}(A)$ is straightforward as described below.

LEMMA 4.3. *If $\prod_{j=1}^{J-1} a_j \neq 0$ then dim $(\mathcal{N}(A)) = 1$ and $\mathcal{N}(A) = sp\,\{\boldsymbol{\nu}^*\}$ for $\boldsymbol{\nu}^* = (1/a_1, \ldots, 1/a_{J-1})^T$. If $\prod_{j=1}^{J-1} a_j = 0$ then the orthonormal vectors $\boldsymbol{e}_k$ with $a_k = 0$ form a basis for $\mathcal{N}(A)$.*

Proof. Suppose $\boldsymbol{0} \neq \boldsymbol{\nu} \in \mathcal{N}(A)$, then it follows from the structure of A that $a_j\,\nu_j - a_{j+1}\,\nu_{j+1} = 0$ for each $j = 1 : J-2$, and so $a_j\,\nu_j = c$ for some constant c. If none of the a_j are zero then the only nonzero solution is $\boldsymbol{\nu} = c\,\boldsymbol{\nu}^*$. If one or more of the a_j are zero then $c = 0$ and so if $a_k \neq 0$ then the corresponding component ν_k of $\boldsymbol{\nu}$ must be zero. ∎

For regions of constant $\mu(x)$ the function $u(x)$ is oscillatory (trigonometric) and hence it is likely that several $a_j \approx u'(x_j)$ will be close to zero, with $\mathcal{N}(A)$ very sensitive to small perturbations. This means that any attempt to eliminate the null vectors $\boldsymbol{\nu}$ from (4.5) using two or more experimental measurements will be doomed to failure. Instead the new SFWI approach combines expressions of the form (4.4) to produce a least squares (overdetermined) system for $\boldsymbol{\mu}$. Suppose that q measurements at a range of frequencies produce the underdetermined systems $A^{(k)}\boldsymbol{\mu} = \boldsymbol{b}^{(k)}$ for $k = 1 : q$. Setting

$$\widehat{A} = \begin{bmatrix} A^{(1)} \\ \vdots \\ A^{(q)} \end{bmatrix} \quad \text{and} \quad \widehat{\boldsymbol{b}} = \begin{bmatrix} \boldsymbol{b}^{(1)} \\ \vdots \\ \boldsymbol{b}^{(q)} \end{bmatrix} \tag{4.7}$$

gives the least squares formulation

$$\min_{\boldsymbol{\mu}\in\mathbb{R}^{J-1}} \left\| \widehat{A}\,\boldsymbol{\mu} - \widehat{\boldsymbol{b}} \right\| ,$$

where $\|\cdot\|$ is the 2−norm. Its solution $\boldsymbol{\mu}_{\rm LS}$ satisfies

$$\widehat{A}^T\widehat{A}\,\boldsymbol{\mu}_{\rm LS} = \widehat{A}^T\widehat{\boldsymbol{b}}$$

(although there are more efficient ways to compute it, see e.g. [11]). We will assume that the matrix $\widehat{A}^T\widehat{A}$ has full rank (in practice this is normally the case even for $q = 2$) and examine the error in $\boldsymbol{\mu}_{\rm LS}$. The (exact) $\mu(x)$ satisfies (4.3) for $j = 1 : J-2$, and we set $\boldsymbol{\mu}_{\rm ex} \in \mathbb{R}^{J-1}$ to be the vector whose jth component is $\mu(x_j)$, and write (4.3) at frequency $\omega = \omega_k$ as $A^{(k)}\boldsymbol{\mu}_{\rm ex} = \boldsymbol{b}^{(k)}$. Stacking these (exact) matrices and vectors as in the approximate case described above then gives the linear system $A\,\boldsymbol{\mu}_{\rm ex} = \boldsymbol{b}$ in $\mathbb{R}^{q(J-2)\times(J-1)}$ which $\boldsymbol{\mu}_{\rm ex}$ solves exactly. This means that
$\widehat{\boldsymbol{b}} - \widehat{A}\,\boldsymbol{\mu}_{\rm ex} = \widehat{\boldsymbol{b}} - \boldsymbol{b} + \left(A - \widehat{A}\right)\,\boldsymbol{\mu}_{\rm ex}$ and so

$$\widehat{A}^T\widehat{A}\,(\boldsymbol{\mu}_{\rm LS} - \boldsymbol{\mu}_{\rm ex}) = \widehat{A}^T\left(\widehat{\boldsymbol{b}} - \widehat{A}\,\boldsymbol{\mu}_{\rm ex}\right) = \widehat{A}^T\left(\widehat{\boldsymbol{b}} - \boldsymbol{b}\right) + \widehat{A}^T\left(A - \widehat{A}\right)\,\boldsymbol{\mu}_{\rm ex}\,. \tag{4.8}$$

It is straightforward to verify that the matrix $\left(\widehat{A}^T\widehat{A}\right)^{-1}\widehat{A}^T$ is bounded by $1/\sigma$ where σ is the smallest singular value of $\widehat{A}$ and this gives the bound

$$\|\boldsymbol{\mu}_{\rm LS} - \boldsymbol{\mu}_{\rm ex}\| \le \sigma^{-1}\,\left(\|\widehat{\boldsymbol{b}} - \boldsymbol{b}\| + \max|\mu(x)|\,\|A - \widehat{A}\|\right)\,.$$

Both norm terms on the right-hand side of this inequality involve the difference between u in (4.3) and its measurement (noise), and the error involved in approximating the derivative and integral terms in (4.5) to obtain the entries in $\widehat{A}$ and $\widehat{\boldsymbol{b}}$ respectively. See also [1] for MRE inversion error bounds.

4.2. SFWI in 2D space. In 2D space $\mu(\boldsymbol{x})$ solves the 2-component system (4.1), and as in 1D we approximate these equations on a staggered grid at different frequencies, stacking up $q > 1$ underdetermined systems into an overdetermined least squares problem. For simplicity we restrict attention to the case for which Ω_1 is the unit square; it is split into a $J \times J$ square mesh and again the components of $\boldsymbol{u}$ are measured at the mesh midpoints (blue stars in Fig. 4.2). The μ nodes are interior edge midpoints (red circles).

Each component of (4.1) is integrated over each interior square (those bounded by red solid lines in Fig. 4.2), with $\Omega_{j,k}$ denoting the $\Delta x \times \Delta x$ square centered at $\boldsymbol{x}_{j+1/2,k+1/2}$. Using the midpoint rule to approximate the left-hand integral and the divergence theorem for the right-hand side gives

$$-\omega^2\Delta x^2 u_\alpha(\boldsymbol{x}_{j+1/2,k+1/2}) \approx \int_{\partial\Omega_{j,k}} \mu\,(u_{\alpha,\beta} + u_{\beta,\alpha})\;n_\beta\,,$$

where $\boldsymbol{n}$ is the outward unit normal. The midpoint rule is used for the four line integrals on the right-hand side, and any corner components of $\boldsymbol{u}$ are obtained by averaging over the four nearest neighbor midpoint values. For example, when $\alpha = 1$ the resulting scheme is

$$\omega^2\Delta x^2 u^1_{j+1/2,k+1/2} = T^1_{j,k}\,\mu_{j,k+1/2} - T^2_{j,k}\,\mu_{j+1,k+1/2} + T^3_{j,k}\,\mu_{j+1/2,k} - T^4_{j,k}\,\mu_{j+1/2,k+1}\,,$$

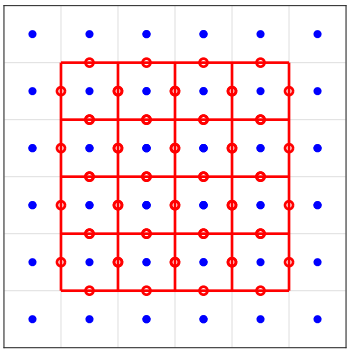

FIG. 4.2. *Staggered grid for 2D approximation of (4.1) on the unit square: the grid points for* $\boldsymbol{u}$ *are denoted by blue stars, and those for* μ *by red circles*

where

$$T^1_{j,k} = 2\left(u^1_{j+1/2,k+1/2} - u^1_{j-1/2,k+1/2}\right), \quad T^2_{j,k} = 2\left(u^1_{j+3/2,k+1/2} - u^1_{j+1/2,k+1/2}\right),$$

$$T^3_{j,k} = u^1_{j+1/2,k+1/2} - u^1_{j+1/2,k-1/2} + \frac{1}{4}\left(u^2_{j+3/2,k+1/2} - u^2_{j-1/2,k-1/2} + u^2_{j+3/2,k-1/2} - u^2_{j-1/2,k-1/2}\right)$$

$$T^4_{j,k} = u^1_{j+1/2,k+3/2} - u^1_{j+1/2,k+1/2} + \frac{1}{4}\left(u^2_{j+3/2,k+3/2} - u^2_{j-1/2,k+3/2} + u^2_{j+3/2,k+1/2} - u^2_{j-1/2,k+1/2}\right),$$

and for simplicity we write $u_\beta(\boldsymbol{x}_{j+1/2,k+1/2})$ as $u^\beta_{j+1/2,k+1/2}$.

In total there are $2\,(J-2)^2$ equations for the $N_J \equiv 2\,(J-1)\,(J-2)$ components of the vector of μ values, and the underdetermined linear system matrix analogous to A in (4.4) is again sparse, with 4 nonzero entries per row. As in 1D we stack up q of these matrix-vector equations, obtained at different frequencies, and calculate its least squares solution $\boldsymbol{\mu}_{\rm LS} \in \mathbb{R}^{2\,(J-1)\,(J-2)}$.

5. Inhomogeneous problem: SFWI results. We now provide numerical test results for the SFWI algorithm using synthetic data in 1D and 2D space. The 1D test results are important in quantifying the algorithm's behavior in the presence of noise because exact solutions to the inhomogeneous problem are not available in higher space dimensions.

5.1. Numerical results for synthetic 1D data. All tests assume that the (exact) $\mu(x)$ is piecewise constant on $[0,1]$ with

$$\mu(x) = \begin{cases} 1\,, & x \in [0,a) \cup (b,1] \\ \mu_I\,, & x \in (a,b) \end{cases} \tag{5.1}$$

and construct the unique $u \in C^1[0,1]$ which satisfies (4.2) subject to given boundary conditions $u(0) = u_L$ and $u(1) = u_R$. These boundary conditions are fixed in some simulations and varied randomly in others. To simulate experimental error we set the nodal u values to be $u_j = u(x_{j-1/2}) + \varepsilon_j\,, \quad j = 1:J\,,$ where again each $\varepsilon_j \in (-\varepsilon, \varepsilon)$ is a pseudo-random noise term. Tests show that varying the interval parameters (a,b) makes little difference to the results and we fix $\underline{\boldsymbol{a = 0.35}}$ and $\underline{\boldsymbol{b = 0.69}}$.

The root mean square (RMS) error in $\mu(x)$ is $\mathcal{E} = \dfrac{\|\boldsymbol{\mu}_{\rm LS} - \boldsymbol{\mu}_{\rm ex}\|}{\sqrt{J-1}}$ and we first investigate how it depends on the inclusion value μ_I for a very accurate approximation

(large J) at multiple frequencies when $\varepsilon = 0$. Fig. 5.1 shows that for high resolution the error $\mathcal{E}$ is at a minimum when $\mu_I = 1$ (i.e. the material is homogeneous), and when $\mu_I > 1$ then $\mathcal{E} \propto \mu_I^2$. Each entry of $\widehat{A}$ in this plot has the same boundary values ($u_L = -1.156$, $u_R = 0.292$), but using boundary values randomly chosen in $[-2, 2]$ makes no observable difference.

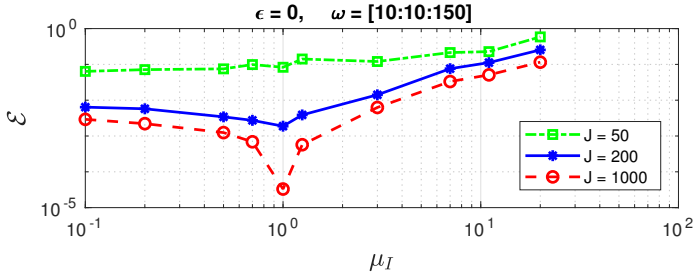

FIG. 5.1. *RMS error in $\mu(x)$ plotted against μ_I using the frequencies $\omega_k = [10 : 10 : 150]$ when $J = 50$ (green dot-dash), $J = 200$ (blue solid) and $J = 1000$ (red dash).*

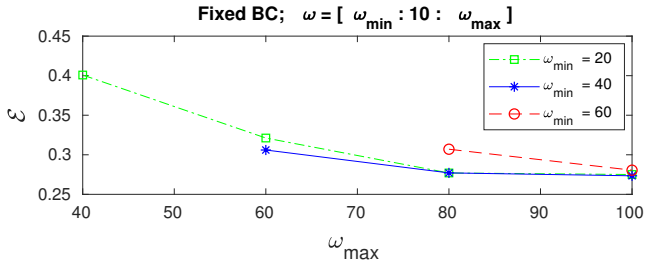

FIG. 5.2. *RMS error $\mathcal{E}$ plotted against the maximum frequency ω_{max} for different values of minimum frequency ω_{min} using the frequencies $\omega_k = [\omega_{min} : 10 : \omega_{max}]$ when $J = 64$ and noise-level $\varepsilon = 0$.*

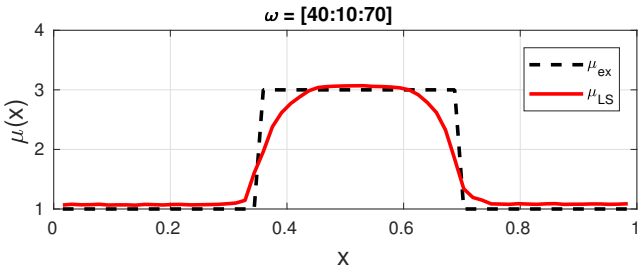

FIG. 5.3. *Plot of calculated $\boldsymbol{\mu}_{LS}$ (red solid line) obtained using $\omega_k = \{40, 50, 60, 70\}$ when $J = 64$ and noise-level $\varepsilon = 0$. The exact value μ_{ex} is shown as a a black dashed line.*

All further test results use a fixed value of $\boldsymbol{\mu_I = 3}$ in order to facilitate comparisons. In the first of these we look at the effect of varying the maximum and minimum frequencies used to generate $\widehat{A}$ and $\widehat{b}$ from (4.7), and results (with $J = 64$, $\varepsilon = 0$ and fixed boundary values) are given in Fig. 5.2. The frequencies $\omega_k = [\omega_{\min} : 10 : \omega_{\max}]$ are used to generate $\widehat{A}$ and $\widehat{b}$, and the graph shows a higher error when

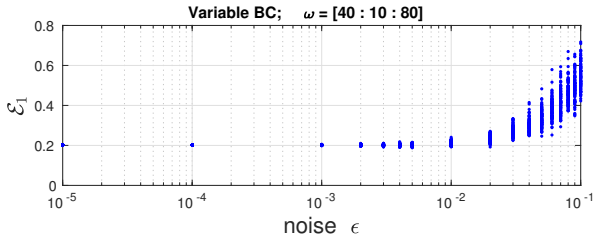

FIG. 5.4. *Plot of L^1-error $\mathcal{E}_1$ in $\boldsymbol{\mu}_{LS}$ against noise-level ε obtained using $\omega_k = [40:10:80]$ when $J = 64$. There are 100 simulations at each value of ε.*

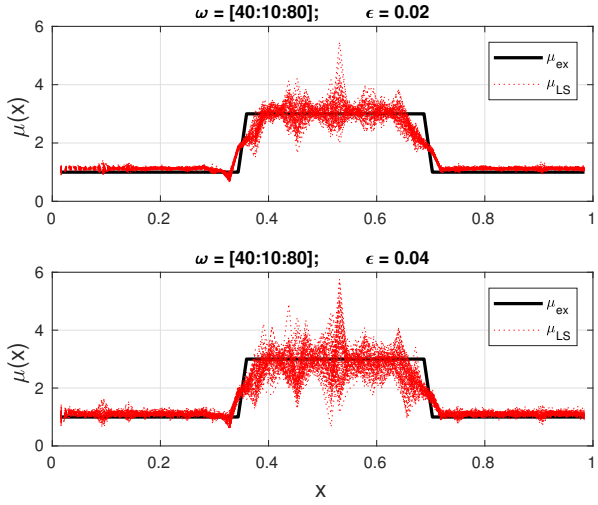

FIG. 5.5. *Plot of 100 simulations of calculated $\boldsymbol{\mu}_{LS}$ (red dotted lines) obtained using $\omega_k = [40:10:80]$ when $J = 64$ and at noise-levels $\varepsilon = 0.02$ (top) and $\varepsilon = 0.04$ (bottom). The exact value μ_{ex} is shown as a a black solid line in each plot.*

$(\omega_{\min}, \omega_{\max}) = (20, 60)$ than $(40, 60)$ even though the first of these includes all the frequencies used by the second. This indicates that including a frequency that is "too low" (relative to the mesh spacing) may make the error worse. Using frequencies that are "too high" (relative to the mesh spacing) can be similarly problematic, giving a solution profile that overestimates the value of μ, and can sometimes be jaggy. The calculated value of $\boldsymbol{\mu}_{\rm LS}$ for "intermediate" frequency values is shown in Fig. 5.3. This plot was generated using fixed boundary values, but using random boundary values gives similar results. Note that the 1D test problem has a low information content compared with 2D (see below), and far higher frequencies need to be used to obtain reasonable results in 1D.

The L^1-norm is a better characterization than $\mathcal{E}$ of the error that is "seen" in a plot like Fig. 5.3 and we define

$$\mathcal{E}_1 = \frac{1}{J-1} \sum_{j=1}^{J-1} \left| \left(\boldsymbol{\mu}_{\rm LS} - \boldsymbol{\mu}_{\rm ex}\right)_j \right| .$$

Fig. 5.4 shows the effect of noise, using randomly varied boundary conditions for u (the plot is the result of 100 simulations at each value of ε) using $\omega_k = [40:10:80]$. Varying the boundary conditions makes little difference, and plots of 100 simulations

for $\boldsymbol{\mu}_{\rm LS}$ at each of $\varepsilon = 0.02$ and $\varepsilon = 0.04$ over these five frequencies with fixed boundary conditions is shown in Fig. 5.5.

5.2. Numerical results for synthetic 2D data. The additional difficulty in 2D simulations is in calculating $\boldsymbol{u}$ for a given inhomogeneous $\mu(\boldsymbol{x})$. This has to be done numerically, and so it is impossible to exactly quantify the noise in a given simulation. All the test results shown below use a piecewise constant $\mu(\boldsymbol{x})$ with background value 1 and value $\mu_I = 3$ in a rectangular inclusion with diagonal corners (0.35, 0.42) and $(0.69, 0.65)$. The function $\boldsymbol{u}(\boldsymbol{x})$ which satisfies (4.1) for this μ is calculated using the MATLAB PDE toolbox on a regular grid of $2\,J_f^2$ triangular elements with $J_f = 256$ (the maximum size allowed by local computer memory requirements), and synthetic noise of size ε is added, as for 1D. For ease of comparison all simulations use the same boundary conditions for $\boldsymbol{u}(\boldsymbol{x})$, corresponding to the same incident wave field. The approximation accuracy of the solution $\boldsymbol{u}(\boldsymbol{x})$ of (4.1) strongly degrades as the nondimensionalized frequency ω increases, but it is notable that calculations using moderate or very low values of ω all give very similar results when $\varepsilon = 0$.

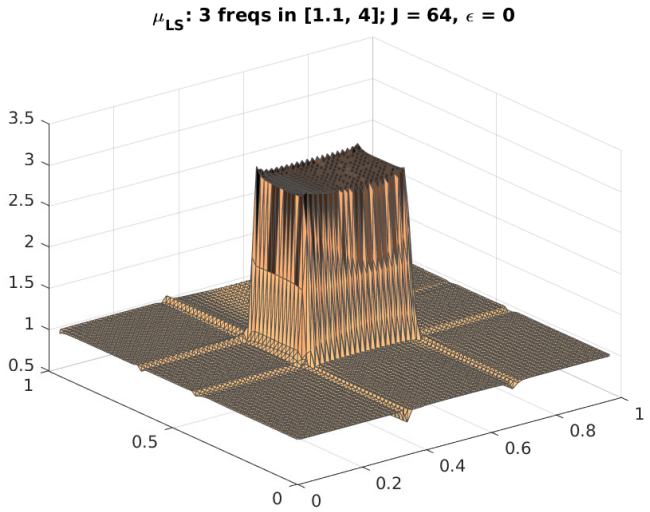

FIG. 5.6. *Plot of $\boldsymbol{\mu}_{LS}$ calculated using $\omega = 1.1, 2.7, 4.0$ when $J = 64$ and $\varepsilon = 0$.*

Fig. 5.6 shows the least-squares solution $\boldsymbol{\mu}_{\rm LS}$ obtained from the three values $\omega = 1.1, 2.7, 4.0$ and sample test results for the L^p errors for $p = 1$, 2 and ∞ when $\varepsilon = 0$ are given in Table 5.1, where the errors are defined as follows:

$$\mathcal{E}_p = \left(\frac{1}{N_J} \sum_{j=1}^{J-2} \sum_{k=1}^{J-1} \left| \mu^{(e)}_{j+1/2,k} \right|^p + \left| \mu^{(e)}_{k,j+1/2} \right|^p \right)^{1/p} \qquad \text{for } p = 1:2$$

and $\mathcal{E}_\infty = \max \left\{ \left| \mu^{(e)}_{j+1/2,k} \right|, \left| \mu^{(e)}_{k,j+1/2} \right| : j = 1 : J-2, k = 1 : J-1 \right\}$, where $\boldsymbol{\mu}^{(e)} = \boldsymbol{\mu}_{\rm ex} - \boldsymbol{\mu}_{\rm LS}$. Although the values of $\mathcal{E}_\infty$ appear very high, this only illustrates that the L^∞ norm is not an appropriate error measure for a discontinuous function: the reconstructed values $\boldsymbol{\mu}_{\rm LS}$ are just slightly offset from the true position, as shown in Fig. 5.7.

ω values used	$\mathcal{E}_1$	$\mathcal{E}_2$	$\mathcal{E}_\infty$
1.1, 2.7, 4.0	0.024	0.122	1.87
4.0, 7.2, 10.0	0.023	0.121	1.72
10, 17.6, 31.2, 40, 50	0.032	0.102	1.72
17.6, 31.2, 40, 50	0.032	0.102	1.72
31.2, 40, 50	0.033	0.103	1.72

TABLE 5.1
Calculated errors in $\boldsymbol{\mu}_{LS}$ using various frequencies when $J = 64$ and $\varepsilon = 0$.

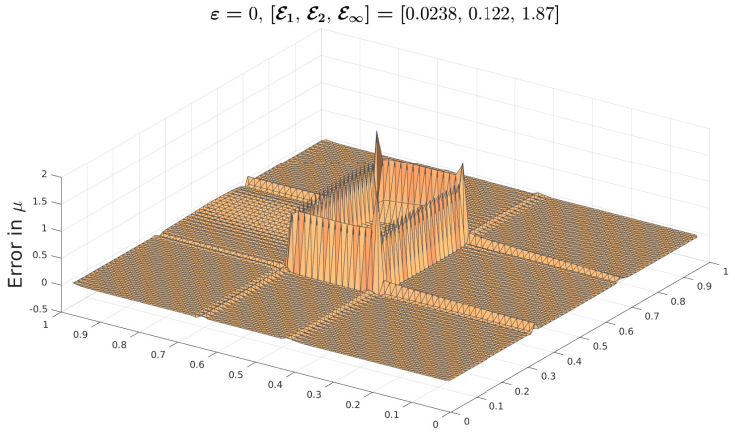

FIG. 5.7. *Plot of error $\boldsymbol{\mu}^{(e)}$ calculated using $\omega = 1.1, 2.7, 4.0$ when $J = 64$ and $\varepsilon = 0$*

Calculations with only low values of ω are very susceptible to added noise, as indicated by Table 5.2. Any values of $\mathcal{E}_1$ larger than about 0.2 correspond to an unacceptably bad solution, and the lower frequency calculations (top two rows) are much worse than this even for $\varepsilon = 10^{-4}$. The results in the bottom three rows are acceptable up to $\varepsilon \approx 0.01$.

ω values used	$\varepsilon = 10^{-4}$		$\varepsilon = 10^{-3}$		$\varepsilon = 10^{-2}$	
$(J = 64)$	$\mathcal{E}_1$	$\mathcal{E}_2$	$\mathcal{E}_1$	$\mathcal{E}_2$	$\mathcal{E}_1$	$\mathcal{E}_2$
1.1, 2.7, 4.0	0.463	0.682	1.074	1.249	1.166	1.292
4.0, 7.2, 10.0	0.059	0.163	0.678	0.946	1.022	1.251
10, 17.6, 31.2, 40, 50	0.032	0.103	0.035	0.105	0.172	0.352
17.6, 31.2, 40, 50	0.032	0.102	0.035	0.105	0.163	0.325
31.2, 40, 50	0.033	0.103	0.036	0.105	0.160	0.322

TABLE 5.2
Calculated errors in $\boldsymbol{\mu}_{LS}$ at three different values of added noise.

6. Discussion and conclusions. Reconstructing the elastic shear modulus $\mu(\boldsymbol{x})$ is a challenging inverse problem even with the rich data source provided by MRE. We have considered two aspects of the problem here: (i) how to use the full time signal instead of a single Fourier component (when μ is constant), and (ii) the overdetermined SFWI method for the inhomogeneous case (in the frequency domain).

MRE measurements are typically taken in small enough space voxels for central differences to give a reasonable approximation of space derivatives, but the relatively coarse timestep size means that an additional assumption of (near) periodicity in time is necessary. The advantages of the Fourier time-interpolant approach (i) are that it uses all the information present in the experimental measurements of $\boldsymbol{u}(\boldsymbol{x}, t)$ and it is guaranteed to give a real value of the real quantity μ. It is well-known that noisy MRE data causes the shear modulus to be underestimated and the numerical test results of Sec. 3 quantify this, showing that the solution is insensitive to low values of additional noise, but that when the noise level exceeds a 'critical' value, then the error in the calculated shear modulus increases rapidly. This critical noise level is proportional to $1/c$ where c is the wave speed in (2.1), and the constant of proportionality in 2D is half that for 1D.

The underlying problem (1.6) is ill-conditioned because the coefficients of the shear modulus can be zero or small, and the SFWI method overcomes this by combining approximations at different frequencies into a single overdetermined matrix–vector equation. Because the individual matrices are derived at different frequencies they have different "problematic" coefficients (i.e. those equal or close to zero) and the overall stacked matrix has full rank if enough frequencies are used. Note that there is a higher information content in the problem as the space dimension increases and so the method should work *better* (i.e. for lower nondimensionalized frequencies) in 3D space than in 2D space (our numerical tests confirm that it works better in 2D space than 1D). This is in contrast to the forward problem of trying to compute the solution $\boldsymbol{u}$ of (1.4) or (1.6) from μ. Our method is designed for MRE inverse problems in which μ is not known anywhere in the material, including at the boundaries. In another type of problem where μ is known somewhere in the material then these values could be be built in as a constraint, or a different formulation might be better.

One obvious extension to the methods described here is to develop a method which uses the SFWI formulation combined with a Fourier interpolant in time for the full time-dependent inhomogeneous reconstruction problem, and this is the focus of current work. Another is to extend our methods to deal with the more sophisticated and accurate model used by McLaughlin et al in [17] in which $p \equiv \lambda \operatorname{div} \boldsymbol{u}$ is taken to be an unknown pressure term in (1.2) and measured values of $\boldsymbol{u}$ are used to determine both μ and p.

The frequency-dependent behavior of μ which is illustrated in Fig. 3.8 is typical (see also [7, Figs 4, 9]) but we have not considered this aspect here, just focusing our attention on (1.4). However it does need to be addressed in further development of methods like SFWI which use measurements obtained at different frequencies. A 'rough and ready' approach could be to use (1.4) but assume that the shear modulus has a specified type of frequency-dependence, e.g. $\mu = (f/f_0)^\alpha \, \mu_1(\boldsymbol{x})$ and then use a similar method to SFWI to obtain μ_1, f_0 and α, but more sophisticated fractional derivative models which take account of the frequency-dependent behavior are available [12]. Another important consideration is the effect of noise and denoising strategies on the calculated result $\boldsymbol{\mu}_{\mathrm{LS}}$. Knowledge of the type of noise present in real measurements is crucial for this: it is likely that the noise in the displacement field $\boldsymbol{u}$ will be temporally and/or spatially correlated to some extent, and an an investigation of models such as the (temporal) Ornstein-Uhlenbeck or (spatial) Q-Wiener processes as described in [6, Sec. 2] may be useful.

REFERENCES

[1] H. Ammari, E. Bretin, P. Millien, and L. Seppecher, *A direct linear inversion for discontinuous elastic parameters recovery from internal displacement information only*, arXiv e-prints, (2018), arXiv:1806.03147, p. arXiv:1806.03147, https://arxiv.org/abs/1806.03147.

[2] H. Ammari, P. Garapon, H. Kang, and H. Lee, *A method of biological tissues elasticity reconstruction using magnetic resonance elastography measurements*, Quart. Appl. Math., 66(1) (2008), pp. 139–175.

[3] H. Ammari, A. Waters, and H. Zhang, *Stability analysis for magnetic resonance elastography*, J. Math. Anal. Appl., 430(2), (2015), pp. 919–931.

[4] S. P. Arunachalam, P. J. Rossman, A. Arani, D. S. Lake, K. J. Glaser, J. D. Trzasko, A. Manduca, K. P. McGee, R. L. Ehman, and P. A. Araoz, *Quantitative 3d magnetic resonance elastography: Comparison with dynamic mechanical analysis*, Magn. Reson. Med., 77(3) (2017), pp. 1184–1192, https://doi.org/10.1002/mrm.26207.

[5] E. Barnhill, P. J. Davies, C. Ariyurek, A. Fehlner, J. Braun, and I. Sack, *Heterogeneous multifrequency direct inversion (HMDI) for magnetic resonance elastography with application to a clinical brain exam*, Med. Image Anal., 46 (2018), pp. 180–188, https://doi.org/10.1016/j.media.2018.03.003.

[6] E. J. Coutts and G. J. Lord, *Effects of noise on models of spiny dendrites*, J Comp. Neuroscience, 32 (2013), pp. 245–257.

[7] F. Dittmann, S. Hirsch, H. Tzschätzsch, J. Guo, J. Braun, and I. Sack, *In vivo wideband multifrequency MR elastography of the human brain and liver*, Magn. Reson. Med., 76 (2016), pp. 1116–26, https://doi.org/10.1002/mrm.26006.

[8] M. M. Doyley, *Model-based elastography: a survey of approaches to the inverse elasticity problem*, Phys. Med. Biol, 57 (2012), pp. R35–R73.

[9] D. B. Duncan and M. A. M. Lynch, *Jacobi iteration in implicit difference-schemes for the wave equation*, SIAM J Num Anal, 28 (1991), pp. 1661–1679.

[10] V. Girault and P.-A. Raviart, *Finite Element Methods for Navier-Stokes Equations*, Springer-Verlag, Berlin, 1986.

[11] G. H. Golub and C. F. V. Loan, *Matrix Computations*, Johns Hopkins University Press, Baltimore, third ed., 1996.

[12] S. Holm and S. P. Näsholm, *Comparison of fractional wave equations for power law attenuation in ultrasound and elastography*, Ultrasound in Med. & Biol., 40 (2014), pp. 695 – 703, https://doi.org/10.1016/j.ultrasmedbio.2013.09.033.

[13] W. Khaled and H. Ermert, *Ultrasonic strain imaging and reconstructive elastography for biological tissue*, in Bioengineering in Cell and Tissue Research, G. M. Artmann and S. Chien, eds., Springer-Verlag, Berlin, 2008, pp. 103–132.

[14] A. J. Laub, *Matrix Analysis for Scientists & Engineers*, SIAM, Philadelphia, PA, 2005.

[15] A. Manduca, T. E. Oliphant, M. A. Dresner, J. L. Mahowald, S. A. Kruse, E. Amromin, J. P. Felmlee, J. F. Greenleaf, and R. L. Ehman, *Magnetic resonance elastography: non-invasive mapping of tissue elasticity*, Med. Image Anal., 5 (2001), pp. 237–254.

[16] C. T. McKee, J. A. Last, P. Russell, and C. J. Murphy, *Indentation versus tensile measurements of Young's modulus for soft biological tissues*, Tissue Engineering: Part B, 17 (2011), pp. 155–164, https://doi.org/0.1089/ten.teb.2010.0520.

[17] J. R. McLaughlin, N. Zhang, and A. Manduca, *Calculating tissue shear modulus and pressure by 2d log-elastographic methods*, Inverse Problems, 26 (2010), 085007 (25 pages), https://doi.org/10.1088/0266-5611/26/8/085007.

[18] E. Park and A. M. Maniatty, *Shear modulus reconstruction in dynamic elastography: time harmonic case*, Phys. Med. Biol., 51 (2006), pp. 3697–.

[19] C. Sánchez, C. Drapaca, S. Sivaloganathan, and E. Vrscay, *Elastography of biological tissue: direct inversion methods that allow for local shear modulus variations*, Image Anal. Recognit., Pt II (2010), pp. 195–206.

[20] L. N. Trefethen, *Spectral Methods in MATLAB*, SIAM, Philadelphia, PA, 2000.